A01-34130

AIAA 2001-3355

A Hall Effect Thruster Plume Model Including Large-Angle Elastic Scattering

I. Katz, G. Jongeward, V. Davis, M. Mandell and I. Mikellides
Science Applications International Corporation
San Diego, CA

R. Dressler
Air Force Research Laboratory, Space Vehicles Directorate
Hanscom, MA

I. Boyd
University of Michigan
Ann Arbor, MI

K. Kannenberg
Lockheed Martin Space Systems Company
Sunnyvale, CA

J. Pollard, The Aerospace Corporation
Los Angeles, CA

D. King
General Dynamics Ordnance and Tactical Systems
Redmond, WA

37th AIAA/ASME/SAE/ASEE
Joint Propulsion Conference and Exhibit
July 8-11, 2001 / Salt Lake City, Utah

AIAA-2001-3355

A HALL EFFECT THRUSTER PLUME MODEL INCLUDING LARGE-ANGLE ELASTIC SCATTERING

Ira Katz*, Gary Jongeward#, Victoria Davis†, Myron Mandell†, Ioannis Mikellides†,
Science Applications International Corporation, San Diego, CA
Rainer Dressler‡, Air Force Research Laboratory, Space Vehicles Directorate, Hanscom, MA
Iain Boyd§, University of Michigan, Ann Arbor, MI
Keith Kannenberg¶, Lockheed Martin Space Systems Company, Sunnyvale, CA
James Pollard¥, The Aerospace Corporation, Los Angeles, CA
David King£, General Dynamics Ordnance and Tactical Systems, Redmond, WA

ABSTRACT

A new model of the plasma plume from Hall Effect Thrusters (HET's) is presented. The model includes the self-expansion of the main beam by density gradient electric fields, low-energy ions produced by resonant charge exchange between beam ions and neutral atoms (ambient and thruster-induced), and angle-dependent elastic scattering of beam ions off neutral atoms. The variation of radial velocities across the annular thruster beam is also included. The model is an advance over previous plume models in the way it numerically models the self-expansion of the main beam, and in particular, the treatment of elastic scattering using recently calculated differential cross sections. The results are compared with recent measurements of the energy and angle-dependent plume from the BPT4000 Hall-Effect Thruster. Both the intensity and energy dependence of the scattering peaks are compared. The principal result is that elastic scattering is the source of the majority of ions with energy greater than E/q=50V that are observed at angles greater than 45° with respect to the thrust axis. The model underscores the need for elastic scattering cross sections for multiply charged ions, as well as a better understanding of HET propellant utilization.

INTRODUCTION

The Hall-Effect Thruster (HET) plume consists mainly of ions generated from two main physical processes. The first is due to energetic beam ions produced and accelerated by the thruster fields. These are the dominant ion species and are the major source of thrust. The second source of ions is due to charge exchange reactions between beam ions and neutral xenon gas. The neutral gas is due to un-ionized particles leaving the thruster and the neutralizer (hollow cathode), and background neutrals present in the vacuum chamber. These reactions have usually been associated with elastic collisions processes that produce low-energy ions at large angles with respect to the main-beam direction. Past empirical and theoretical work has focused mainly on these two components.[1,2,3]

---

* Chief Scientist, Senior Member AIAA
# Division Manager, Member AIAA
† Sr. Staff Scientist, Member AIAA
‡ Task Scientist, Member AIAA
§ Associate Professor, Senior Member AIAA
¶ Senior Engineer, Member AIAA
¥ Senior Scientist, Member AIAA
£ Chief Scientist, Member AIAA

PLUME MEASUREMENTS

Experiments conducted by The Aerospace Corporation[4] for Lockheed Martin Space Systems Company on the Busek-Primex, Hall-Effect Thruster (BPT-4000, Figure 1), provided data for comparisons with computer models. The comparisons were made for discharge power and potential of 3kW and 300V, respectively. Measurements were taken using fully exposed flux probes ("uncollimated") for assessing the non-directional ion flux, and probes inside graphite collimators ("collimated").[4] Figure 2 shows data using a collimator of energy spectra at different angles with respect to the thruster axis. The angle-independent, high-energy peak at E/q~280V associated with the main beam is clearly evident. Conversely, the characteristic small-amplitude, charge-exchange ion peaks are demonstrated at the lowest energy values of the collimated spectra. The charge exchange peak is more evident in the uncollimated data of Figure 3. The resonant charge exchange between beam ions and neutrals has a relatively large cross-section (~55 $Å^2$)[5] and produces low energy ions of E/q~20V at 45° (90° center-of-mass). Figure 2 further reveals the existence of secondary current density peaks, with relatively high energies compared to the primary resonant charge exchange peak. For example, at an angle of 40° the energy associated with the second maximum is approximately 150V. These observed ion-flux crests show a marked energy dependence on angle. Because the energy dependence is roughly given by $E_b\cos^2\theta_{lab}$, where E_b is the main ion beam energy and θ_{lab} is the angle with respect to the thruster axis, we associate these ions with elastic scattering (momentum transfer) events. These observations prompted numerical modeling of all pertinent plume processes to further elucidate the observed trends.

PLUME MODELING

Main Beam Expansion.

Based on previously published reports, there appears to be agreement on the physics that control the expansion of the main ion beam from the thruster.[3, 6] However, for modeling purposes, it is extremely difficult to prevent numerical "grid" and "shot" noise from distorting the results when standard PIC algorithms are employed. Noise in the calculations manifests itself by increasing the concentration of high-energy beam particles at large angles. Qualitatively, the numerical noise mimics the (large-angle) elastic scattering alluded to earlier. However, it is erroneous, quantitatively, in both amplitude and particle energy. Ions scattered by xenon atoms have a definite relationship between energy and scattered angle. Particles scattered by grid noise, do not obey the same laws.

A Lagrangian algorithm has been employed to calculate the expansion of the main beam. The primary beam is assumed to be comprised of a collisionless, singly-ionized, quasi-neutral plasma expanding in a density-gradient electric field. The electron drift velocity is small compared to the electron thermal speeds, thus momentum balance is assumed:

$$m_e \frac{d\mathbf{v}_e}{dt} = e\nabla\phi - \nabla p = 0 \qquad (1)$$

where, $\mathbf{v}_e$, ϕ and p are the electron velocity, electric potential and electron pressure, respectively. The electron mass is m_e and the charge is e. By assuming ideal gas behavior this leads to a *barometric* potential law,

$$\phi = T_e \ln\left(\frac{n}{n_\infty}\right) \qquad (2)$$

with T_e being the electron temperature, n is the plasma density (n_e=n_i) and n_∞ is a reference plasma density. The plume is also assumed to be isothermal. This is a better approximation for space conditions than in the laboratory, where inelastic collisions with background neutrals will cool the electrons.

Ions are accelerated by the electric fields,

$$m_i \frac{d\mathbf{v}_i}{dt} = -e\nabla\phi \tag{3}$$

Since the drift velocity of the ions, **V**, is much greater than their thermal velocity, the high velocity ions are modeled as a fluid, $\mathbf{V} = \mathbf{v}_i$). The governing equations, solved in 2-D (R-Z) geometry, are conservation of mass and momentum:

$$\nabla \cdot n\mathbf{V} = 0$$
$$m_i \mathbf{V} \cdot \nabla \mathbf{V} = -\frac{\nabla p}{n} \tag{4}$$

The accuracy of the algorithm has been confirmed by comparisons of analytical solutions[7,8] with model problems in one and two dimensions.

The Lagrangian modeling approach leads to a reduced numerical noise (Figure 4, right). The latter is usually associated with PIC algorithms, especially in cases where large changes in scale sizes are not adequately resolved, and when statistical particle fluctuations (*shot noise*) overwhelm the physical forces (Figure 4, left). Moreover, without incredibly fine zoning and large numbers of particles, PIC is not accurate enough to predict ion trajectories in problems with large scale ratios (e.g. fractions of a millimeter to several meters). However, unlike PIC, the fluid technique assumes a mono-energetic beam. A multi-energy beam could be simulated using a superposition of ion fluids, but was not performed in the present effort. Finally, PIC requires considerably longer computational times (e.g. minutes of real time on an 800MHz PC versus tens of hours of CPU time on parallel IBM SP/SP2 processors).[3]

Neutral Gas Density.

The neutral gas density in a laboratory vacuum chamber has three components: un-ionized beam particles, un-ionized neutralizer gas (from the hollow cathode), and a background density. The beam of neutrals from the thruster is computed using an annular anode gas flow model with isotropic emission from the ring. This is done by calculating two disk emissions, one large and one smaller, and subtracting the smaller from the larger. The density drop off with r and z from a disk emitting a Maxwellian is calculated using an approximate view factor (Appendix B). Energetic CEX neutrals are negligible compared to the total neutral density and are therefore not included in the model.

The hollow cathode neutrals are assumed to have an isotropic emission at a constant temperature, equal to cathode orifice temperature (538°C was taken as the assumed value for the BPT-4000). The neutralizer is offset from the thruster by a distance r_{HC} from the axis of symmetry. Since there are an equal number of points from the thruster axis closer to and farther from the neutralizer, the cylindrically averaged neutral density for any point at a distance z downstream is estimated as if the point was along the thruster centerline (see Appendix B).

The chamber background density is assumed to be constant. Based on values of the ambient temperature and pressure the background density is determined assuming an ideal gas law. The value of background pressure for the plume calculations was taken to be 3e-5 torr, and is higher than measured by about a factor of three but consistent with integrated current and performance measurements. It is noted that the measured values were obtained using ionization gauges placed at each end of the chamber (upstream and downstream of the thruster), close to the re-entrant cryopumps.[4] No background density is assumed at space conditions. Figure 5 shows the three components of the neutral density for the BPT-4000 and the total computed value.

Neutral-Ion Interactions.

Charge-exchange (CEX) is computed using a two-dimensional, R,Z-geometry PIC code. The main beam ion densities computed by the Lagrangian calculations, and the neutral gas profile, were used as input. The charge exchange ion density is calculated by tracking particle trajectories in density-gradient electric fields using a finite-current barometric law for the electron

density (electron current equals ion current). The code solves Poisson's equation on a finite element grid and iterates until steady state CEX densities and density-gradient potentials are self-consistent. Previous comparisons of the CEX plume model with flight data from the NSTAR's ion engine exhibited good agreement.[1]

Figure 6 shows one-meter plume maps calculated for the BPT-4000 under both lab and space conditions. The CEX density in the lab is found to be more than one order of magnitude greater than it is in space due to the dominance of the background neutral gas in the chamber. By comparison with measurements of the integrated ion current (5-6Amps for collector potential of 20V),[4] the computed CEX ion current is overestimated in the laboratory case (5.3Amps) due to the fact that the model does not account for the depletion of main beam ions. The calculation employed a cross-section that was based on the calculations and measurements by Pullins et al.[5] The value implemented, assuming 300V ions, was 55 Å^2.

The distinctive second peak in the energy spectra (Figure 2) captured by the collimated retarding potential analyzer (RPA) data prompted additional computations. Compared to the low-energy, charge-exchange ions expected to be present at the higher angles (Figure 3), the observed peak in both collimated and uncollimated RPA data suggests the existence of processes, not previously modeled, that produce additional ions. The relatively high values of energy, at angles where the main beam ions are not expected to be a major contributor, further substantiate this notion.

We have calculated differential cross section data for elastic Xe^+-Xe scattering in a center-of-mass frame of reference. The calculations involve averaging over the pertinent Xe_2^+ potentials, without inclusion of charge exchange. The results are corrected for charge exchange subsequently. The complete analysis is presented in Appendix A.

The derived, center-of-mass differential cross sections were converted to values in a fixed frame of reference relative to the laboratory and implemented in the plume model (Appendix A). The cross sections shown in (Figure 7) are calculated for pure elastic scattering without including charge exchange. For direct comparisons with RPA measurements the flux of scattered ions F_{es}, may be estimated (using mean value theorem) by,

$$F_{es} = \int_0^{x_c} \frac{dF}{dx} dx = \int_0^{x_c} \frac{I_b n_o}{d^2} \frac{d\sigma}{d\Omega} dx \approx \frac{I_b n_o x_c}{d^2} \frac{d\sigma}{d\Omega}\bigg|_{x_c} \qquad (5)$$

and is computed at a radius of 1m (the RPA location). In expression (5) above, I_b and n_o are the main beam ion current and neutral density, respectively. The characteristic dimensions used in the approximation are shown below along with the RPA collimator acceptance angle (12.25deg).

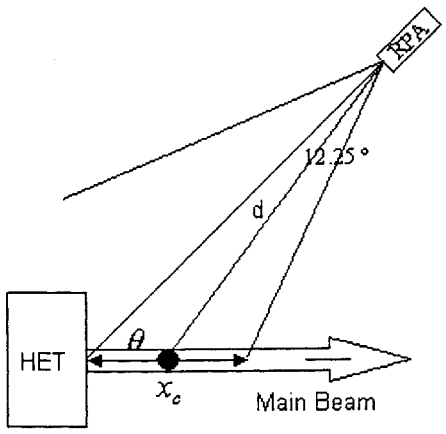

The differential contribution due to the column element along the beam is denoted by dx and $d\sigma / d\Omega$ is the differential cross section in the lab frame evaluated at x_c.

COMPARISONS

Results from the plume calculations using the scattering cross-section treatments described above were compared with RPA measurements. In order to draw conclusions specifically about the elastic-scattering ion production source, comparisons were performed using a reduced set of RPA data. Specifically, the high-energy part was removed by fitting a smooth curve to the higher-energy data points and subtracting it form the total ion current (Figure 8).

Figure 9 shows separately the computed ion flux (eqn (5)) using the unutilized propellant from the thruster only, and both thruster and chamber neutral density. The first was estimated based on the assumption that all the neutral gas was generated 0.1m above the thruster centerline. The corresponding column density was calculated as 1.8e17 m^{-2}. The background density was estimated to be 1.06e18 m^{-3}. The fraction reaching the detector after accounting for losses due to charge exchange was assumed to be approximately 60% at 1m and scaled inversely with distance.

Figure 10 shows the same comparison after implementing an initial radial spread in the beam velocity. The value (8 km/s) was based on measurements from the SPT-140 thruster conducted at The Aerospace Corporation.[9] It is evident that the addition of the spread greatly improves the comparison with measurements. One additional comparison is shown in Figure 11. Here, the maximum computed ion energy compares well with values from the RPA measurements (the values for 55° and 65° are rough estimates from broad peaks).

Finally, the results from the complete calculation are compared with data in Figure 12. Profiles include the expanded beam ions only, beam and scattered ions, and all three components combined. Also plotted are the ion current probe data for four bias levels: 50V, 100V data with no collimator. As expected the beam-only values compare best with the ion probe biased to 100V, since at this value most of the scattered and charge exchanged ions are excluded. Conversely, the values combining beam and elastic scattering compare well with 50V-biased probe data since this excludes most of the charge exchange ions. As expected, the total electron density, measured at a radial location of 56cm, is in good agreement with values computed without the elastic-scattering formulations (Figure 14). As already mentioned, although the energy of ions associated with small-impact parameter elastic scattering is relatively high, their density compared to the principal large-impact parameter charge-exchange component is small (0.05-1 order of magnitude less at angles >45°).

CONCLUSIONS

A plume model has been developed to explain observed trends in the BPT4000 Hall-Effect thruster. The main beam expansion is calculated using a fluid technique in which ion trajectories serve as streamlines. This technique avoids the grid noise that is commonly associated with particle-in-cell (PIC) models. The low-energy ions from charge-exchange collisions however, are computed using a PIC method, with relatively high characteristic collision cross section (~55Å^2). Finally, recently computed differential cross-sections have been implemented in the model to account for elastic collisions that result from ion-neutral interactions at very short interatomic distances (i.e. small impact parameters). Both the computed intensity and energy dependence of the scattering peaks have been compared with measurements. These recent calculations, using the more recent differential cross-sections, require a more rigorous analysis. Nevertheless, the relatively good agreement with empirical values exposes the importance of elastic scattering as a source of highly energetic ions. While these ions account for only a few percent of the beam they are found to be the principle energetic ions, with energies exceeding E/q~100V at angles higher than 45° with respect to the thruster axis. At such high energies these large-angle scattered ions pose a concern for a variety of S/C surface interaction issues (e.g. erosion from sputtering).

ACKNOWLEDGMENTS

This work was supported by the Lockheed Martin Space Systems Company. RAD acknowledges support from AFOSR under task 2303EP02 (Michael Berman and Mitat Birkan, program managers).

APPENDIX A
Formulation for Xenon Ion Differential Cross-Sections.

The differential cross sections associated with an atomic collision can be calculated from the deflection function, $\Theta(E_T,b)$[10]

$$\Theta(E_T,b) = \pi - 2b\int_{R_m}^{\infty} \frac{dR}{R^2[1-b^2/R^2 - V(R)/E_T]^{\frac{1}{2}}} \quad (6)$$

where E_T is the center-of-mass collision energy, b is the impact parameter, R is the interatomic distance, R_m is the trajectory turning point (point of nearest approach) and $V(R)$ is the interatomic potential energy. A typical deflection function is shown in Figure 14. Note, that the observed scattering angle, θ, is given by:

$$\theta = |\Theta|, \quad 0 < \theta < \pi \quad (7)$$

Thus, at $|\Theta|<\theta_r$, where θ_r is the so-called rainbow angle corresponding to the minimum in the deflection function, the differential cross section, $I(\theta,E_T)$, has three contributing impact parameters. The differential cross section is obtained from:

$$I(\theta,E_T) = \frac{d\sigma}{d\Omega} = \left|\frac{b}{\sin\theta(d\theta/db)}\right| \quad (8)$$

where the solid angle, dΩ, is given by $d\Omega=2\pi \sin\theta\, d\theta$. The deflection function in Figure 14 was calculated for the $^2\Sigma_u^+$ potential of the $Xe^+ + Xe$ collision system and a collision energy of 3 eV.

The corresponding differential cross section is shown in Figure 15. Noted is the discontinuous behavior at the rainbow angle, corresponding to a singularity in the classical differential cross section, and the high cross sections at lower scattering angles. In reality (quantum scattering), the rainbow singularity observed in the differential cross section is smoothed out due to the wave properties of the collision system. At higher energies, the deflection function barely exhibits a minimum, the scattering is essentially only governed by the repulsive part of the interaction potential, and the classical approach is sufficiently accurate. At the energies of interest in the present work, this is the case.

The calculation of the angular cross sections boils down to knowledge of the interaction potentials. The relevant Xe_2^+ potentials without spin-orbit interaction, calculated by Amarouche and coworkers,[11] is shown in Figure 16.

For the present collision energies, the spin-orbit interaction can be neglected because the spin-orbit potentials approach the spin-orbit free potentials at small inter-atomic distances. The $Xe^+ + Xe$ scattering is caused by the inter-atomic potentials of two charge-transfer pairs, a Σ and a Π system. The differential cross section at a particular angle, θ, is given by:

$$I(\theta) = \tfrac{1}{3} I(\theta,\Sigma) + \tfrac{2}{3} I(\theta,\Pi) \quad (9)$$

In the case of the Π potential scattering, the charge-transfer pair, Π_g and Π_u, are well represented by Morse potentials:

$$V(R) = D_e\{\exp(2\beta(R_e - R)) - 2\exp(\beta(R_e - R))\} \quad (10)$$

The deflection function (eqn. 6) is calculated from the average Π potential, which is also given by a Morse potential. The Morse potential parameters derived from the averaged potentials by Amarouche et al.[11] are listed in Table 1.

Potential	D_e(eV)	β(Å^{-1})	R_e(Å)	σ(Å)	n
Π_{u-g}	0.096	1.34	4.19		
Σ_g^+				2.11	6.57
Σ_u^+	1.384	1.297	3.162		

Table 1. Potential parameters used for the differential cross section calculations.

In the case of the Σ potentials, the $^2\Sigma_u^+$ potential is the attractive potential representing the ground electronic state of the system, while the $^2\Sigma_g^+$ potential is purely repulsive. Consequently, a simple analytical expression for the average potential does not exist. We have, therefore, calculated the differential cross section for the individual Σ states using the potential parameters listed in Table 1.

The repulsive potential was obtained by fitting the $^2\Sigma_g^+$ potential to the functional form (in eV):

$$V(R) = 27.21\left(\frac{\sigma}{R}\right)^n \tag{11}$$

A correct implementation of small angle scattering requires an assumption for the total elastic cross section. A frequently applied approach is:

$$\sigma_{tot} = 2\sigma_X \tag{12}$$

where σ_{tot} is the total elastic cross section and σ_x is the charge-exchange cross section. This is reasonable since the charge exchange probability becomes oscillatory below a critical impact parameter, b_c, for which $\sigma_x = 0.5\ \pi\ b_c^2$. Another approach, leading to slightly higher total cross sections, is to calculate the charge-transfer probability, $P_X(b)$, and conduct the differential cross section calculations for all impact parameters below a limiting value for which a significant charge exchange probability is calculated. It is also important to implement the correct charge-exchange cross section as given by the measurements and calculations of Pullins et al.[5]

The differential cross sections must meet following condition:

$$2\sigma_X = 2\pi \int_0^{b_c} I(\theta)\sin\theta \mathrm{d}\theta \tag{13}$$

Equation (8) does not differentiate between charge exchange and pure elastic scattering processes. It merely provides the differential cross sections of the "mass scattering". At angles $\theta > \theta(b_c)$, the differential cross sections for ions in an ion-neutral charge-exchange pair such as $Xe^+ + Xe$, is calculated from:

$$I_{ion}(\theta) = \tfrac{1}{2} I(\theta) + \tfrac{1}{2} I(\pi - \theta) \tag{14}$$

Regarding the accuracy of the derived differential cross sections, it must be emphasized that the potentials, to which analytical expressions have been fit, were calculated in the vicinity of the chemical interaction (see Figure 16). However, large angle scattering depends on the interaction at very short interatomic distances, as can be seen from the respective small impact parameters in the deflection function. Consequently, the calculated differential cross sections are sensitive to the applied functional form representing the repulsive part of the potential.

Frame Transformation

The most general elastic collision process between two particles of unequal masses m_1 and m_2, velocity vectors before the collision, $\mathbf{v}_1$ and $\mathbf{v}_2$, and after the collision, $\mathbf{v}_1'$ and $\mathbf{v}_2'$, can be represented by the geometrical construction in Figure 17 (left) using the definitions,

Relative velocities: $\mathbf{V} = \mathbf{v}_1 - \mathbf{v}_2$, $\mathbf{V}' = \mathbf{v}_1' - \mathbf{v}_2'$
Center-of-mass vel.: $\mathbf{v}_{cm} = (m_1\mathbf{v}_1 + m_2\mathbf{v}_2)/(m_1+m_2)$
Reduced mass: $M = m_1 m_2/(m_1+m_2)$

In the case of equal masses and one stationary particle the geometric construction reduces to the illustration above (right) where θ_L and θ_{cm} are the deflection angles in the laboratory and center-of-

mass frames, respectively. It can then easily be shown that,

$$2\theta_L + (\pi - \theta_{cm}) = \pi \Rightarrow 2\theta_L = \theta_{cm} \qquad (15)$$

The center-of-mass differential cross sections can then be converted into the laboratory frame of reference as follows:

$$\begin{aligned}\frac{\partial \sigma}{\partial \Omega_L} &= \frac{\partial \sigma}{\partial \Omega_{CM}} \frac{\partial \Omega_{CM}}{\partial \Omega_L} \\ &= \frac{\partial \sigma}{\partial \Omega_{CM}} \frac{\sin\theta_{CM}\, d\theta_{CM}}{\sin\theta_L d\theta_L} \\ &= \frac{\partial \sigma}{\partial \Omega_{CM}} \frac{\sin 2\theta_L\, 2\, d\theta_L}{\sin\theta_L d\theta_L} \\ \frac{\partial \sigma}{\partial \Omega_L} &= \frac{\partial \sigma}{\partial \Omega_{CM}} 4\cos\theta_L \end{aligned} \qquad (16)$$

APPENDIX B

Formulas used for estimating the neutral distribution in the plume model.

Thruster Neutrals

The profile of neutrals from the thruster is computed using two disk emissions and subtracting the smaller from the larger:

$$\theta_1(r_o, r, z) = r_o \tan\left(\frac{r + r_o}{z}\right) - r_o \tan\left(\frac{r}{z}\right)$$

$$\theta_2(r_o, r, z) = -r_o \tan\left(\frac{r - r_o}{z}\right) + r_o \tan\left(\frac{r}{z}\right)$$

$$\bar{x}(r_o, r, z) = \sqrt{1 + \frac{r^4}{r_o^4} + \frac{z^4}{r_o^4} + \frac{2z^2}{r_o^2} - \frac{2r^2}{r_o^2} + \frac{2r^2 z^2}{r_o^4}}$$

$$x(r_o, r, z) = \frac{r^2 + z^2 + r_o^2 (1 - \bar{x})}{2r}$$

$$\theta_3(r_o, r, z) = r_o \sin\left(\sqrt{\frac{r_o^2 - x^2}{r^2 - 2rx + r_o^2 + z^2}}\right)$$

$$\Omega(r_o, r, z) = \frac{\sqrt{\left(1 - \frac{\cos(\theta_1) + \cos(\theta_2)}{2}\right)\left(1 - \cos(\theta_3)\right)}}{2}$$

$$n_{HET}(r, z) = \frac{2F_o\left(\Omega(r_o, r, z) - \Omega(r_i, r, z)\right)}{m_i u_o \pi\left(r_o^2 - r_i^2\right)} \qquad (17)$$

where, F_0 is the neutral flow rate, u_0 is the neutral speed at the thruster exit and m_i is the particle mass. The inner and outer radii of the acceleration channel are denoted by r_i and r_o, respectively.

Neutrals from the Hollow Cathode

The hollow cathode is offset by a distance r_{HC} from the thruster. The constant-temperature neutrals are emitted isotropically from the neutralizer. Their distribution $n_{HC}(z)$ is estimated based on,

$$n_{HC}(z) = \frac{F_{o,HC}}{\pi m_i u_{o,HC}} \frac{z}{(\max[r_{HC}, r]^2 + z^2)^{3/2}} \qquad (18)$$

where, $F_{o,HC}$ is the mass flow rate and $u_{o,HC}$ is the particle speed.

REFERENCES

[1] Davis, V.A., et al., "Ion Engine Generated Charge Exchange Environment: Comparison Between NSTAR Flight Data and Numerical Simulations," AIAA Paper 2000-3529, July 2000.

[2] Samanta Roy, R.I., Hastings, D.E., and Gatsonis, N.A., "Numerical Study of Spacecraft Contamination and Interactions by Ion-Thruster Effluents," *Journal of Spacecraft and Rockets*, Vol. 33, No. 4, 1996, pp. 535-542.

[3] VanGilder, D.B., Boyd, I.D., and Keidar, M., "Particle Simulations of a Hall Thruster Plume," *Journal of Spacecraft and Rockets*, Vol. 37, No. 1, 2000, pp. 129-136.

[4] Pollard, J.E., et al., "Ion Flux, Energy, Charge-State Measurements for the BPT-4000 Hall Thruster," AIAA Paper 01-3351, July, 2001.

[5] Pullins, S., Dressler, R.A., Chiu, Y., and Levandier, D.J., "Ion Dynamics in Hall Effect and Ion Thrusters: $Xe^+ + Xe$ Symmetric Charge Transfer," AIAA Paper 00-0603, January, 2000.

[6] David Y. Oh, et al., "Modeling of Stationary Plasma Thruster-100 Thruster Plumes and Implications for Satellite Design," *Journal of Propulsion and Power,* Vol. 15, No. 2, 1999, pp. 345-357.

[7] Parks, D.E., and Katz, I., "A Preliminary Model of Ion Beam Neutralization," IEPC Paper 79-2049, October 1979.

[8] Ashkenazy, J., and Fruchtman, A., "Far Field Analysis of the Hall Thruster Plume," Division of Plasma Physics (DPP) and International Congress on Plasma Physics (ICPP) Meeting, Quebec City, Canada, BM1.004, October, 2000.

[9] Pollard, J.E., and Beiting, E.J., "Ion energy, ion velocity, and thrust vector measurements with the SPT-140 hall thruster," 3rd International Conference on Spacecraft Propulsion, 10-13 Oct 2000, Cannes, France.

[10] Child, M., *Molecular Collision Theory*, Academic Press, London, 1974.

[11] Amarouche, M., Durand, G. and Marlieu, J.P., "Structure and Stability of Xe_n^+ Clusters," *J. Chem. Physics*, Vol. 88, 1988, pp. 1010-1018.

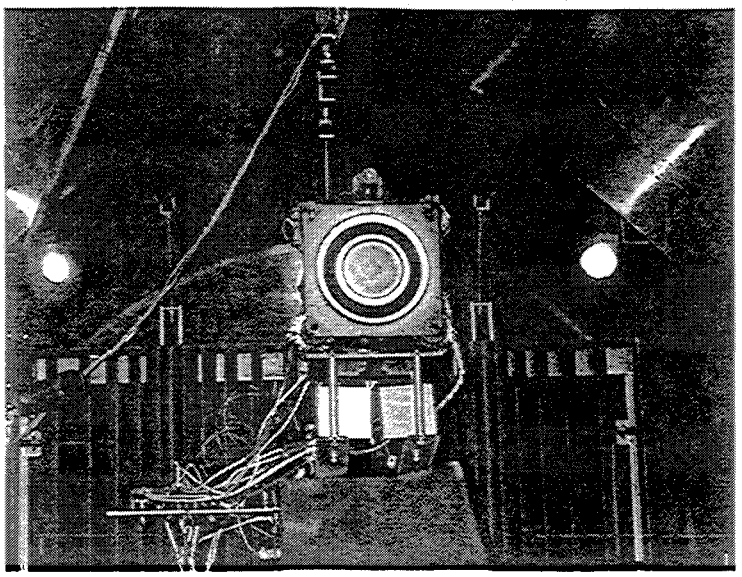

Figure 1. The BPT-4000 Hall-Effect Thruster.

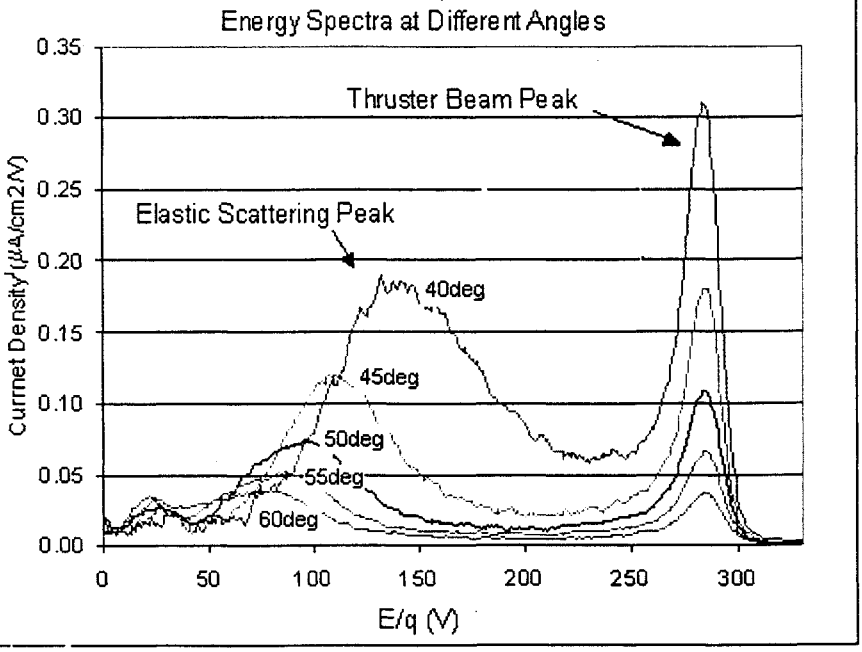

Figure 2. Collimated RPA data for the BPT-4000 at discharge power of 3kW and and voltage of 300V showing the angle-independent, high-energy main beam peaks and the angle-dependent, elastic scattering peaks (data taken at The Aerospace Corporation by Jim Pollard et al.).

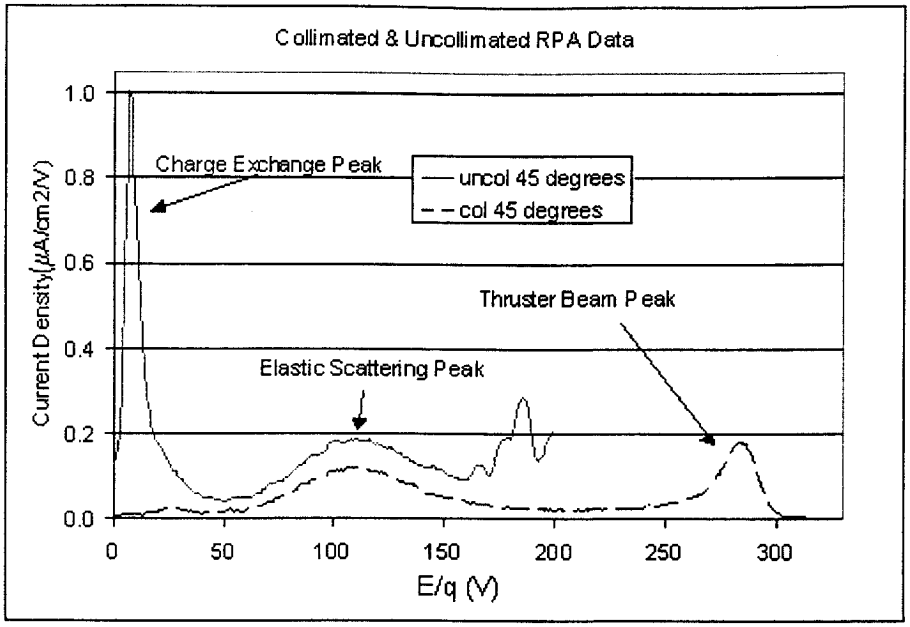

Figure 3. RPA measurements at 45° from the BPT-4000 discharge power of 3kW and and voltage of 300V showing a large, low-energy, charge-exchange ion peak in the uncollimated data (taken at Aerospace Corporation by Jim Pollard et al.).

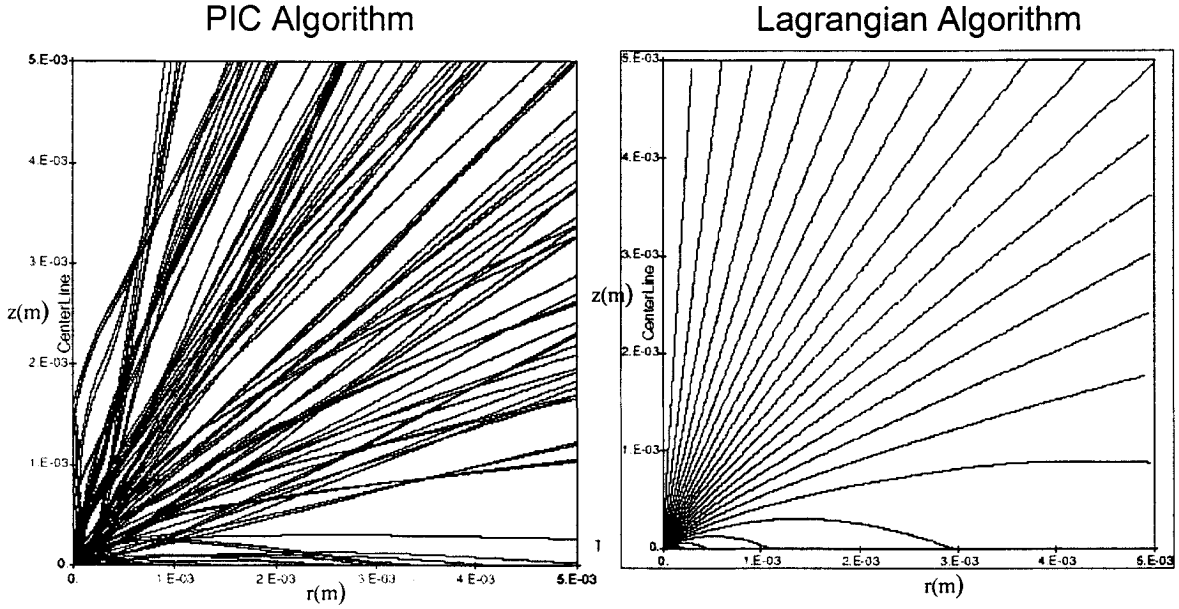

Figure 4. Comparison of ion trajectories using PIC and Lagrangian calculation techniques.

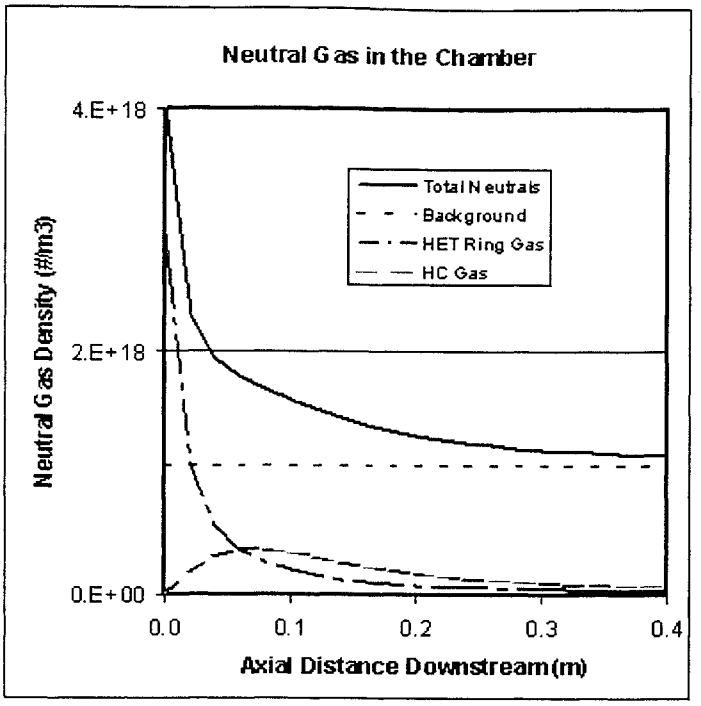

Figure 5. Neutral gas density downstream of the BPT 4000 exit plane.

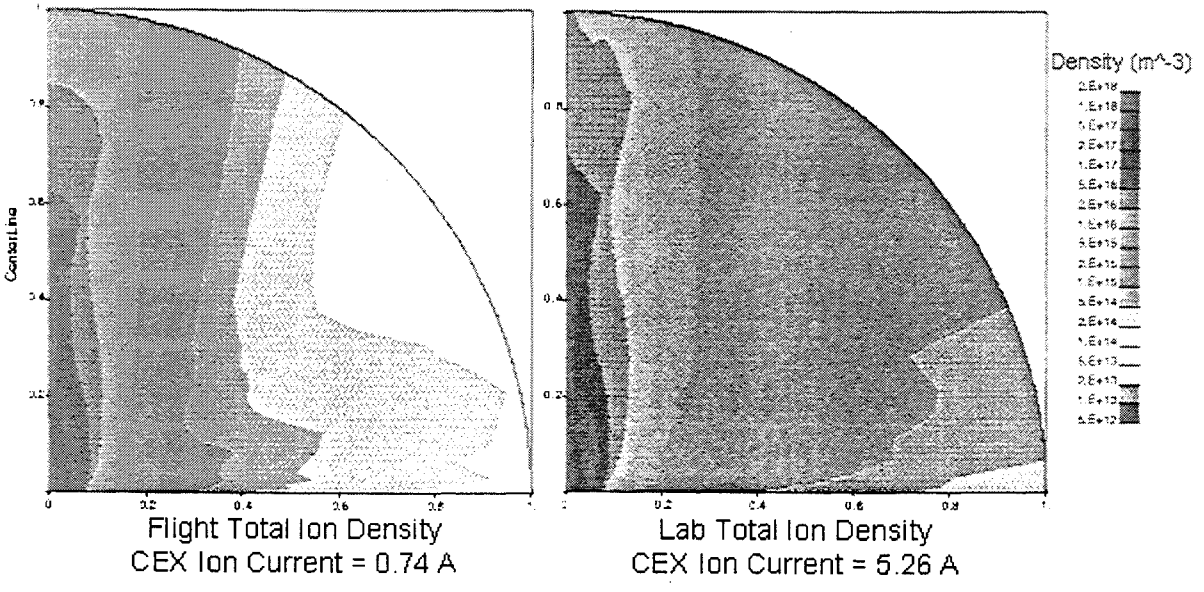

Figure 6. HET plume maps for lab and space conditions showing dominance of background density in the charge-exchange plume production.

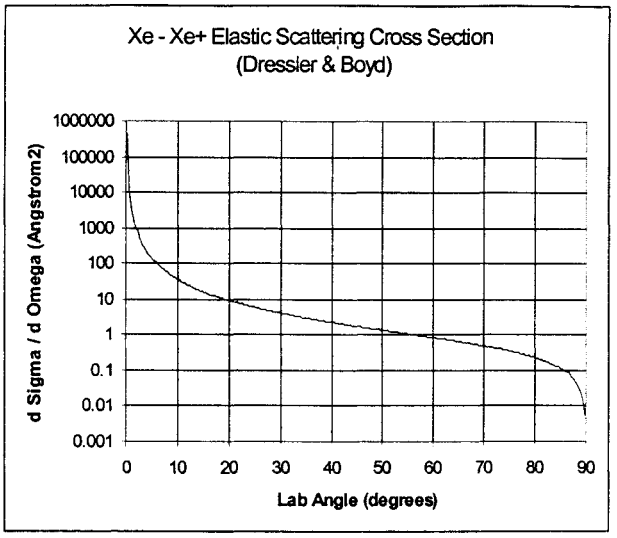

Figure 7. Differential cross sections for xenon ion-neutral scattering in the laboratory frame of reference.

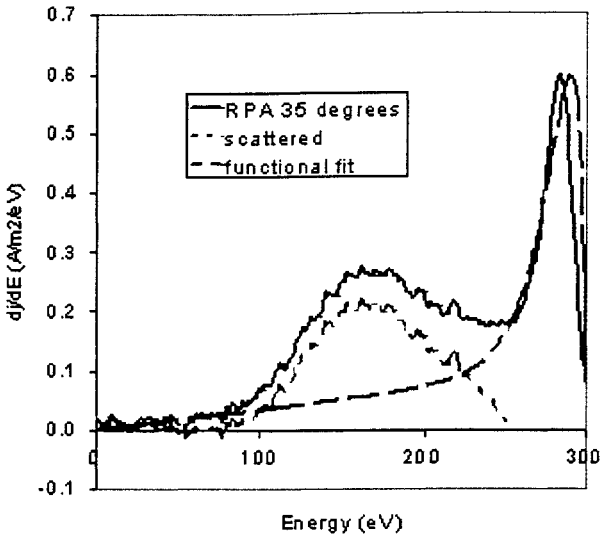

Figure 8. RPA data with fit of high energy only. Difference between the two profiles is the scattered component.

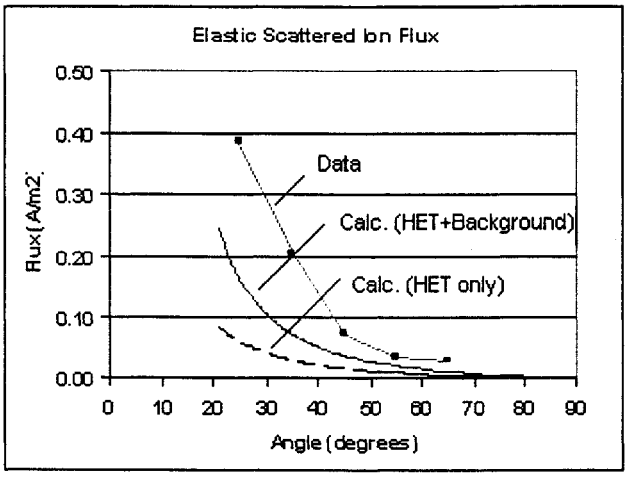

Figure 9. Scattering contribution calculated using the recent cross sections and neutral densities from the BPT-4000 thruster only (dashed line). Computed flux using both thruster and chamber gas is also shown (solid line). Both profiles are compared with the scattering-only contribution from the RPA data.

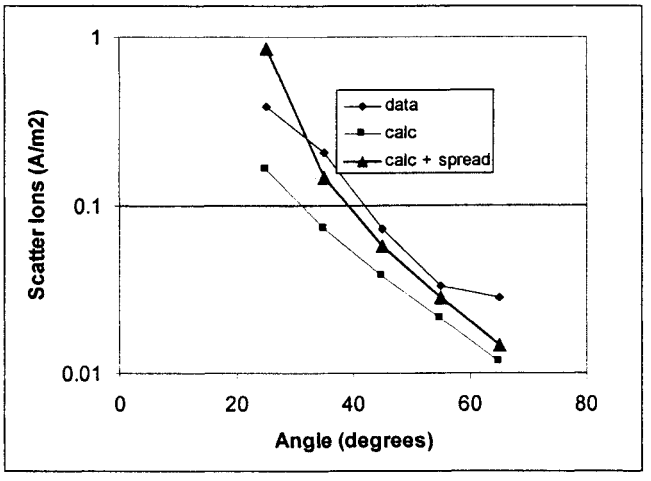

Figure 10. Comparison between measured and computed scattered ion fluxes, with and without the spread in the radial component of the initial beam velocity.

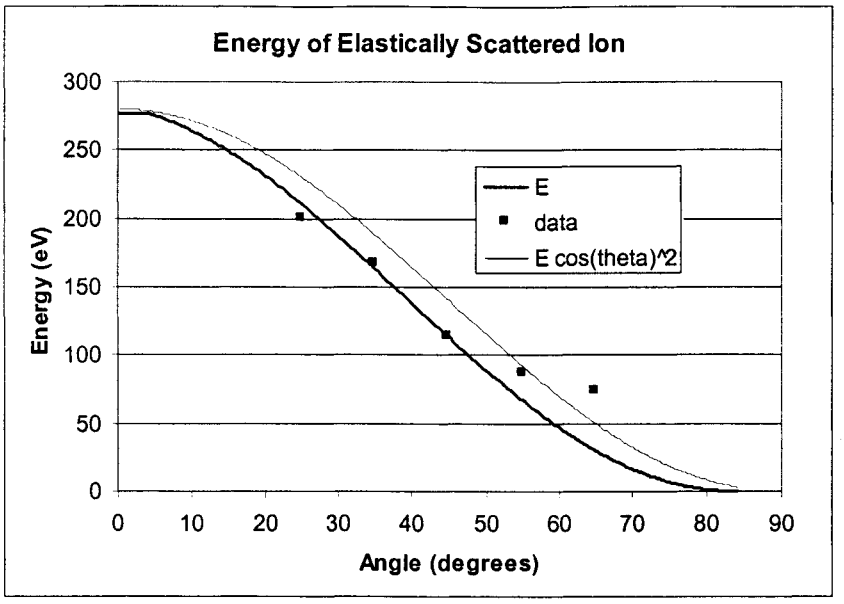

Figure 11. Comparison between calculated and measured ion energies. Also shown as reference is the E $\cos^2(\theta)$ energy dependence on angle (in the lab frame of reference).

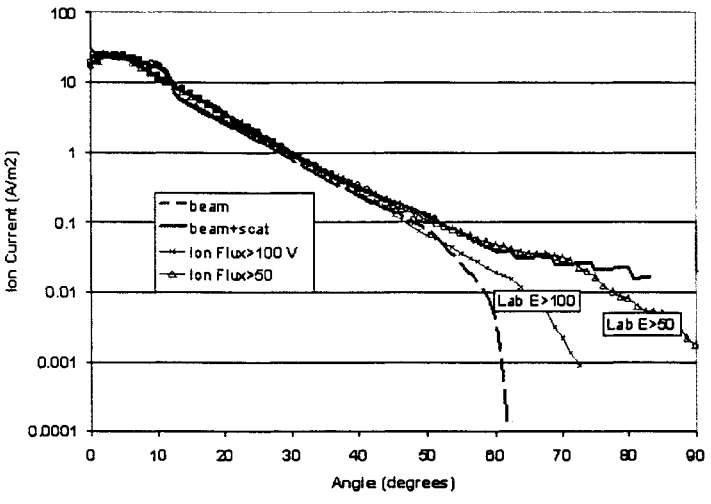

Figure 12. Comparison of high-energy ion current between calculations and measurements for the BPT-4000.

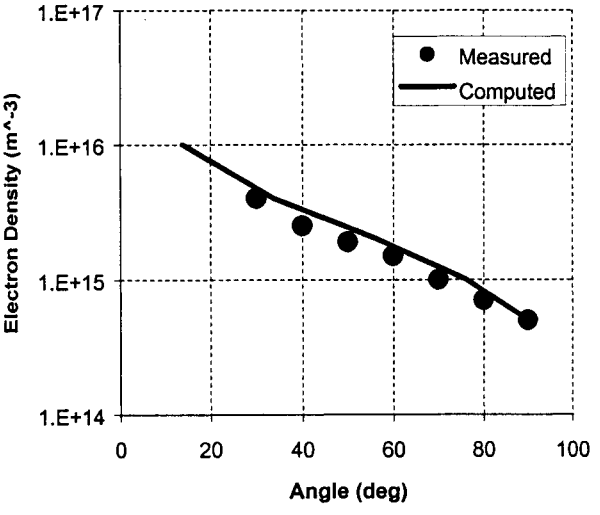

Figure 13. Comparison of measured and computed electron densities (w/o elastic scattering) for the BPT-4000. (Radial location: 56cm)

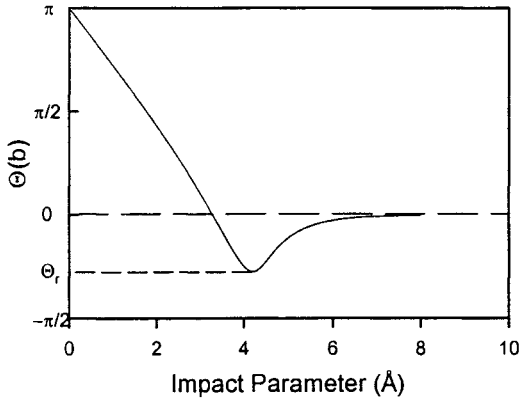

Figure 14. Deflection function for the Xe_2^+ $^2\Sigma_u^+$ Morse potential, as defined in Table 1, and calculated for a collision energy of 3 eV (c.m.).

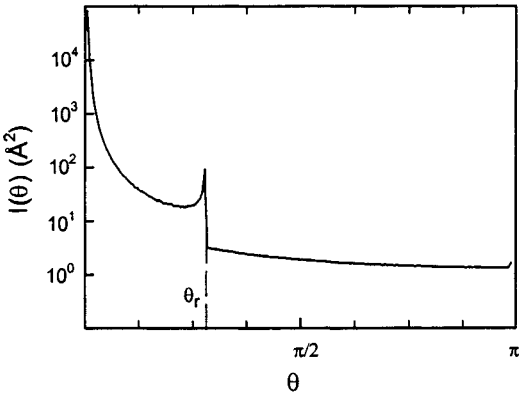

Figure 15. Differential cross section calculated from the deflection function of Figure 14.

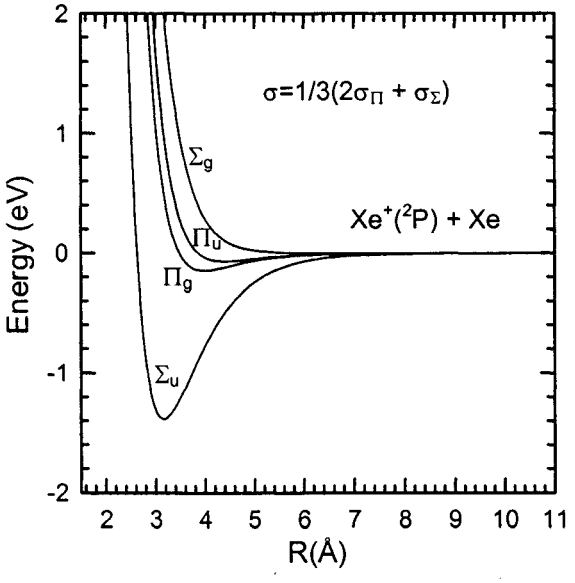

Figure 16. Spin-orbit free Xe2+ potentials as calculated by Amarouche et al.[11]

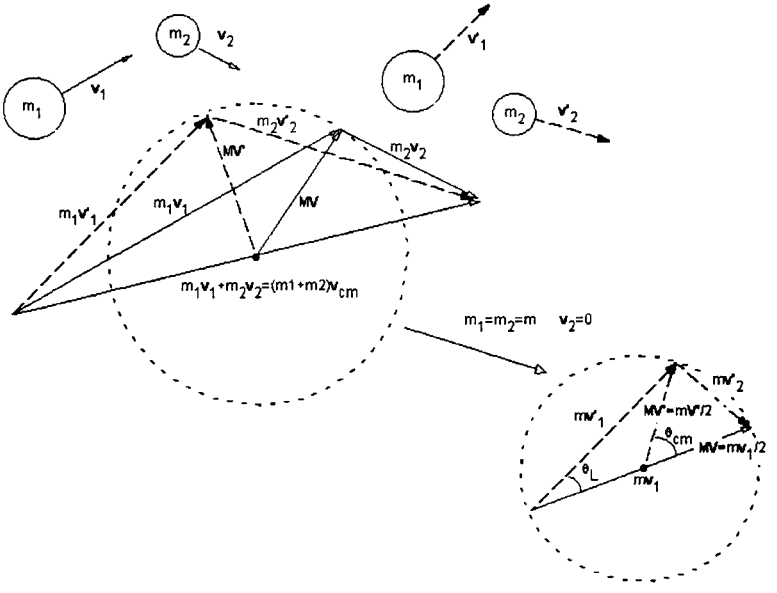

Figure 17. Geometrical construction of the general elastic collision process (left) reduced to the simplified construction on the right for equal masses and one stationary particle.